THE JOURNAL OF PHYSICAL CHEMISTRY C

Subscriber access provided by MINCyT

C: Surfaces, Interfaces, Porous Materials, and Catalysis

Kinetics and Mechanism of the Hydrogen Peroxide Reduction Reaction on a Graphite Carbon Nitride Sensor

Mariana Isabel Rojas, Oliviero Andreussi, Cesar G. Gomez, and Lucia Bernardita Avalle

J. Phys. Chem. C, **Just Accepted Manuscript** • DOI: 10.1021/acs.jpcc.9b07315 • Publication Date (Web): 03 Dec 2019

Kinetics and Mechanism of the Hydrogen Peroxide Reduction Reaction on a Graphite Carbon Nitride Sensor

Mariana I. Rojas[1]*, Oliviero Andreussi[2], Cesar G. Gomez[3], Lucía B. Avalle[4]

[1]Universidad Nacional de Córdoba (UNC), Facultad de Ciencias Químicas, Departamento de Química Teórica y Computacional. Instituto de Investigaciones en Fisicoquímica de Córdoba (INFIQC-CONICET). Ciudad Universitaria, 5000 Córdoba, Argentina.

[2]University of North Texas (UNT), Department of Physics, TX 76203 Denton, USA.

[3]Universidad Nacional de Córdoba (UNC), Facultad de Ciencias Químicas, Departamento de Química Orgánica. Instituto de Investigación en Ingeniería de Procesos y de Química Aplicada (IPQA-CONICET). Ciudad Universitaria, 5000 Córdoba, Argentina.

[4]Universidad Nacional de Catamarca (UNCa), Facultad de Ciencias Exactas y Naturales, Av. Belgrano 300, K4700 San Fernando del Valle de Catamarca, Catamarca, Argentina. Instituto de Física Enrique Gaviola (IFEG-CONICET), Ciudad Universitaria, 5000 Córdoba, Argentina.

Supporting Information

ABSTRACT: The kinetics and mechanism of the hydrogen peroxide reduction reaction (HPRR) on a recently proposed carbon-based electrode is studied by means of experiments and simulations. The electrode is Highly Oriented Pyrolytic Graphite (HOPG) modified by the deposition of a graphite carbon nitride (g-C_3N_4) film. Current transients obtained from chronoamperometry measurements allow us to propose a kinetic model for the HPRR on the surface. The model produces excellent fits of current transients, providing sensible rate constants for each electro-catalytic step. The rate constants obtained are consistent with low energy barriers for each step, suggesting outstanding electro-catalytic activity of the g-C_3N_4/HOPG electrode. Moreover, different trends are found for low and high analyte concentration, evidencing a change in the reaction mechanism. In order to clarify the mechanisms involved in the reaction, first principles atomistic simulations were performed. The different reaction steps were modeled at the substrate/water interface, including solvent environment through continuum embedding approaches. The simulated thermodynamics and kinetics of the different processes show that a significant role in the electrocatalytic activity of the system is associated to the geometrical rearrangements of the interface, with a critical role played by the corrugation / de-corrugation processes of the outermost sheet of the electrode.

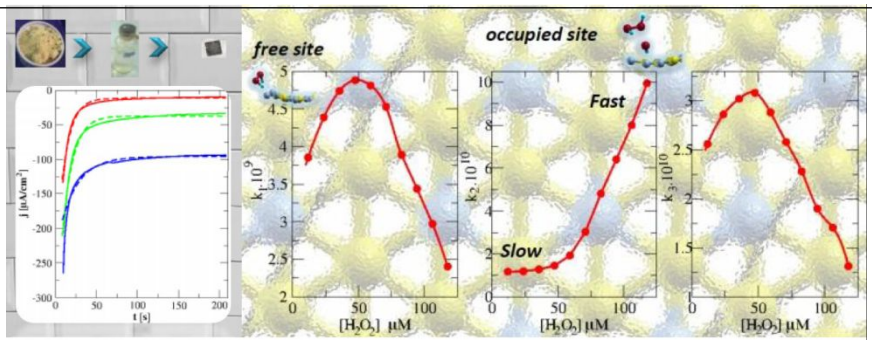

INTRODUCTION

Accurate detection and quantification of H_2O_2 is important due to its essential role in the food industry, environmental protection, and medical diagnoses[1-2]. The importance for biochemical analysis is also evident, as H_2O_2 is the product of several biological enzyme-catalyzed reactions[2-7]. In this context, carbon materials represent ideal candidates for the manufacture of (bio)sensors, due to their large surface area and low commercial cost. Among the carbon-based electrodes that have been proposed for this task we can mention highly oriented pyrolytic graphite(HOPG)[8-10], graphene[11], carbon nanotubes (CNTs)[12], graphene nano-ribbons (GNRs)[13-14], graphite carbon nitride (g-C_3N_4)[15-21], and graphene with hydrogenated pores (GPH)[22].

g-C_3N_4 is a new variety of binary carbonaceous material composed of carbon and nitrogen. It is a non-polluting material obtained by polymerization from an N-rich precursor, with low production cost. Since the atoms composing the material belong to different groups of the Periodic Table, they form different numbers of bonds, resulting in a periodic distribution of pores in the honeycomb network. Two allotropic forms of g-C_3N_4 are known so far, composed of either triazine or tri-s-triazine units. The synthesis of the latter is easier[18].

Recently, by means of quantum mechanics studies, we have characterized the properties of the two allotropes of g-C_3N_4, both in sheets (2D) and crystals (3D)[19]. The structures, the different types of stacking, the adhesion between sheets, the porosity of the material, and the electrical properties were studied. In addition, X-ray diffraction patterns (XRD) and electron transmission microscopy (TEM) were also simulated[19]. Moreover, a comprehensive study on the synthesis and characterization of g-C_3N_4 employed in the manufacture of g-C_3N_4/HOPG sensor was performed, including the characterization of the electrode performances

for the HPRR[20]. The experimental results showed that the g-C_3N_4 film on HOPG had a surprising electro-catalytic activity due to the presence of tri-s-triazine units, composed of C and N atoms with sp^2 hybridization. The measurement showed that the g-C_3N_4/HOPG sensor exhibited outstanding response compared to that exhibited by pristine HOPG[18-21]. In the tri-s-triazine units, there are three different types of N atoms, all with different surroundings. Two of the three N types have the lone pair in a *p* orbital and the third N type has the lone pair in an sp^2 orbital, allowing H-bond interaction and favoring adsorption of H_2O_2. The differences observed in adsorption energies (E_{ads}) between the HOPG surface (-0.05 eV / molecule)[23] and g-C_3N_4 / HOPG (-0.86 eV / molecule)[20] were correlated with the low ($\Theta \rightarrow 0$) and high ($\Theta \rightarrow 1$) coverages found in the two electrodes respectively.

The characterization of the electrocatalytic activity of the g-C_3N_4/HOPG sensor requires a thorough understanding of the electrochemical environment, where HPRR takes place. The overall electrocatalytic process is the result of a subtle balance between different substrate-adsorbate interactions, alternative reaction mechanisms, electron transfer processes, and environment effects due to interactions with the embedding solvent and unwanted ion adsorption from the electrolyte. Another source of practical difficulty in the investigation of the overall electrocatalytic process is linked to the proper account of mass transport. In terms of experimental probes, cyclic voltammetry (CV) is frequently used to characterize the electrocatalytic activity of an electrode. Although this technique can provide first qualitative insights, more precise measurements are required for a quantitative analysis. Thus, electrochemical impedance spectroscopy (EIS) and current density transients can be performed to study the kinetics of the electrochemical reactions[20].

Although the above characterization techniques provide useful kinetics information, they do not give us descriptive information about the species involved in the mechanism. The aim of the present work is to elucidate the kinetics and mechanisms of HPRR on g-C_3N_4/HOPG sensor, by combining new experimental data with accurate first-principles simulations that account for the complex electrochemical environment. In particular, recent advances in the field of continuum models of solvation in condensed matter simulations allow us to include solvent and electrolyte effects in a partially periodic system, such as the two-dimensional interface of an electrocatalytic device, at a significantly reduced computational cost[24].

This work is organized as follows. After a short discussion of the experimental and simulation techniques adopted, a kinetic model for the electrocatalytic process is proposed and experimental transients are fitted accordingly. The trends of the rate constants at low and high concentration are analyzed. In the second part, the mechanism of HPRR is studied by means of quantum mechanical calculations of the interfacial electrocatalytic steps, embedded in a continuum solvation environment. Adsorption energies, reaction free energies, and minimum energy paths (MEP) for each elementary step are analyzed, allowing characterization of the thermodynamic and kinetic details of each mechanism.

EXPERIMENTAL

A conventional electrochemical cell of three electrodes is used, consisting of a working electrode g-C_3N_4/HOPG[20] with an exposed area of 0.2827 cm^2. The g-C_3N_4 film is deposited on HOPG PSI 7mm x 7 mm x 1mm surface from an ethanolic suspension, dropwise, followed by ethanol evaporation. We use $Ag/AgCl$ as a reference electrode and a gold rod (Alfa Aesar 99.9985% purity) as an auxiliary electrode. The electrolyte is 0.2 M phosphate buffer pH 7, Anedra (Argentine). Oxygen-free solution is obtained by continuously purging the electrochemical cell with nitrogen gas (99.999% purity). Water from a Milli-Q-Millipore System is used for the preparation of all solutions and for glassware cleaning.

Stabilization of the system is performed by applying an initial potential, V_i of -0.40 V. A potential step at a more negative potential value, V_{trans} of -0.6 V, is then applied recording the current as a function of time. Afterwards, the potential is returned to the initial value. The electrochemical analyser used is a Metrohm AUTOLAB-PGSTAT302N potentiostat (Switzerland), equipped with a staircase scan module and electrochemical interface using the Nova 2.01 software package.

COMPUTATIONAL METHODS

All Density Functional Theory (DFT) calculations are performed using the Quantum ESPRESSO package[25-26]. The van der Waals interactions are considered within the Grimme dispersion corrections. The Kohn-Sham orbitals and charge density are expanded in a plane-wave basis set with energycutoffs of 40 Ry and 320 Ry respectively. Ultrasoft pseudopotentials are employed with the Perdew-Burke-Ernzerhof (PBE) approximation for exchange and correlation functional[27-29]. The Brillouin zone is sampled with a 4x4x1 irreducible Monkhorst-Pack k-point grid[30]. The convergence threshold for the total energy at each electronic calculation is set to $1x10^{-8}$ Ry. Geometry optimizations are performed by employing the Broyden-Fletcher-Goldfarb-Shanno (BFGS) algorithm; total forces acting on each ion are minimized until smaller than $1x10^{-3}$ Ry/a.u. The MEPs for the different steps of the HPRR is computed using the Nudged Elastic Band method (NEB)[31-33]. Free energies are approximated by the total ground state energies of the systems, neglecting vibrational contribution.

The HOPG substrate is modeled as composed of three sheets of graphite of 18 carbon atoms each and disposed following the standard honeycomb lattice. The graphite carbon nitride film deposited on the HOPG is represented by a single sheet, composed of 8 nitrogen and 6 carbon atoms. An AB stacking sequence is selected, corresponding to a tetragonal simulation cell of 7.29 Å x 7.29 Å x 30 Å. Periodic boundary conditions (PBC) in the plane directions are enforced, while a parabolic correction on the orthogonal direction is adopted to decrease PBC artefacts[34] while reducing the size of the simulation cell. Figure 1 shows the optimized structure of the slab. The distance between g-C_3N_4 and graphene sheets is 3.20 Å, while the distance between sheets in the graphite is 3.35 Å. The flat structure of the sheets validates a view of the pristine electrode in which all atoms have ideal sp^2 hybridization.

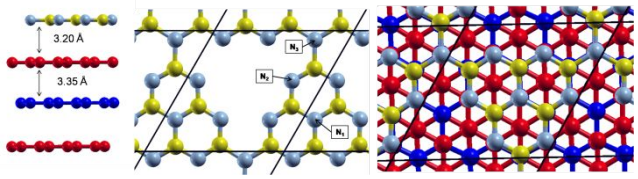

Figure 1. (Left) Side view of the g-C_3N_4 / graphite substrate shows the inter-planar distance. (Center) Top view of the g-C_3N_4 sheet. There are three inequivalent N atoms. (Right) Top view of the g-C_3N_4 /graphite substrate. Continuous black line indicates the unit cell 7.29 Å x 7.29 Å x 30 Å.
C: yellow spheres; C: red spheres; C: blue spheres N: gray spheres.

In modeling the HOPG/g-C_3N_4/water interface, solvent is represented by using an implicit solvation approach. Among different recently proposed models, the Self-Consistent Continuum Solvation (SCCS) model by Andreussi et al.[35] was adopted, as implemented in the Environ v1.0 library for the Quantum ESPRESSO package. In this approach, the interface between the quantum-mechanical solute and the surrounding continuum environment is described by a smoothly varying function of the electronic density of the solute[35]. Electrostatic screening by the solvent is described following a polarizable dielectric model, which requires the efficient solution of a generalized Poisson equation[36]. Non-electrostatic (e.g. cavitation, dispersion, repulsion, etc.) interactions between the solute and the continuum solvent are accounted for in SCCS by defining them as proportional to the quantum-surface and, possibly, the quantum-volume of the solute[24]. While most of the different interaction terms were shown to play a crucial role in reproducing solvation free energies of individual compounds in water[35], it is important to underline the fact that for the electrocatalytic reactions in this study we expect the main contribution to be of electrostatic nature.

RESULTS AND DISCUSSION

1. Interface Characterization

The surface of g-C_3N_4 polymer behaves like a buffer so that the pH of the solution may affect the acid-base character by protonation/de-protonation. It is known that the point of zero charge (PZC) of g-C_3N_4 particles in aqueous suspension occurs at pH_{PZC} 5.2[37-38]. This value is almost similar to that obtained by Zhu *et al.* for the isoelectric point (IEP) of g-C_3N_4 through ζ-potential measurements[39], reporting a value of pH_{IEP} 5. Since in our case the electrolyte is a buffer of pH 7, we expect the g-C_3N_4 sheet to be negatively charged.

Open-circuit potential (E_{OCP}) measurements provide information on the interface before the flow of current through the cell. E_{OCP} vs. time transients are registered in a lapse of time of 200 seconds at different concentrations. Figure 2 shows that the E_{OCP} increases with concentration. This picture is consistent with a slow process of H_2O_2 adsorption taking place on the surface until equilibrium is reached. The E_{OCP} blank value (-0.046 ± 0.001 V) is not included in the graph.

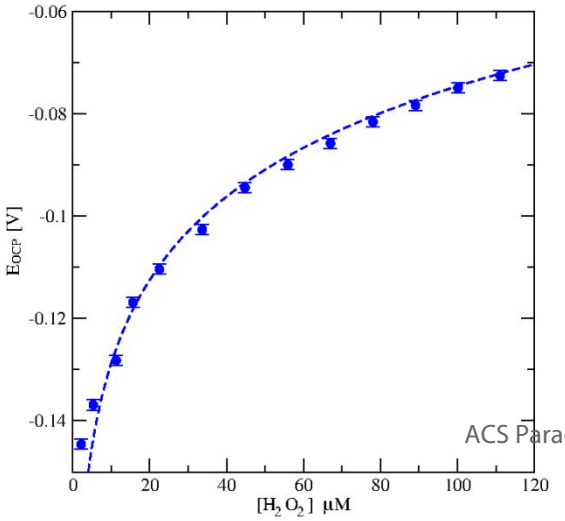

Figure 2. E_{OCP} vs. $[H_2O_2]$ for HOPG/g-C_3N_4 working electrode with buffer pH 7 electrolyte and Ag / AgCl reference electrode. (Dashed line) Langmuir-type isotherm behavior.

Even though we do not have spectroscopic measurements that allow elucidating the structure of the double layer, it is worth reporting that a similar behavior has been previously observed by Lv *et al.* for a different substrate[40]. In their work, Sum Frequency Generation (SFG) spectroscopy was exploited to study the adsorption of H_2O_2 on the quartz/water interface as a function of the concentration. The adopted spectroscopic technique allowed detecting the ordering of molecules at the interface that arises through hydrogen-bond (H-bond) interactions. In their system, the addition of H_2O_2 displaced H_2O molecules, due to the higher propensity of H_2O_2 to form H-bonds with the substrate. H_2O_2 is thus shown to behave as a more effective proton donor than H_2O, owing to its lower pKa value (11.6 and 15.7 for H_2O_2 and H_2O, respectively). After the adsorption of a first layer of H_2O_2 on the surface is observed, with the increase of concentration a second change on H-bond interactions is detected, caused by the formation of a second layer of H_2O_2 located at greater distance from the surface[40].

When the potential was applied, both Chronoamperometry (CA) and Electrochemical Impedance Spectra (EIS) measurements evidenced a change in the kinetics of the HPRR with the concentration[20], indicating a change in the mechanism of the reaction.

2. Electrochemical Characterization of the HPRR

2.1Kinetic Model

Transients of current density provide a very accurate probe of the electrocatalytic reactions, but do not allow characterizing the fine details of the intermediate species involved in each step of the HPRR. To help identifying the elementary steps, a kinetic model must be devised, capable of connecting all the information available. In particular, as the reduction reaction involves the transfer of two electrons, there must be at least two elementary steps. The proposed kinetic model is based on the following assumptions:

Two consecutive reductive steps are followed by a non-electrochemical one.

The rate of the first reductive step depends on the number of free sites on the surface.

The rate of the second reductive step depends on the number of occupied sites.

The last non-electrochemical step is related to the release of the site.

By further neglecting double layer charging, transport contribution and the reverse reactions, the above kinetic model allows us to express the current density of the transient measured at a given over-potential η step for the HPRR as:

$$j(t) = -n_1 F k_1 (1-\theta(t)) - n_2 F k_2 \theta(t) \quad (1)$$

where $k_1$and k_2 are the rate constants of the two electrochemical steps, F is the Faraday constant equal to 96,485 C/mol, and n_1 and n_2 are the number of electrons involved in the two reductive steps, namely $n_1 = n_2 = 1$.

The evolution of the surface coverage with time θ can be described according to:

$$\theta = 1 - \exp(-\lambda t) \quad (2)$$

where λ is given by:

$$\lambda = \frac{nFk_3}{\rho} \quad (3)$$

and is a function of the analyte concentration through the rate constant of the site release (k_3), ρ is the charge density of active sites (assumed to be 2.78x10^{-4} C/cm^2) and $n = 1$.

2.2 Kinetic Parameters

Figure 3 (Left) shows in solid lines the experimental transients of currents at three different concentrations registered at a potential of -0.6 V vs. $Ag/AgCl$ reference electrode. As expected, the cathodic current increases in absolute value with the analyte concentration. Dashed lines show the corresponding fitting with the kinetic model. Figure 3 (Right) shows the coverage θ as function of time. The largest differences observed on the surface coverage with the analyte concentration appear at short times, while at longer times the surface is fully covered in all cases. As H_2O_2 concentration increases, the molecular order at the interface is modified by new H-bond interactions[40].This behavior makes it increasingly difficult to free the site, producing a delay in this step.

The values of the k_i constants, with $i = 1, 2, 3$ for the different steps, were obtained from the fit between the kinetic model and the experimental transients using the simplex algorithm[41]. Figure 4 shows how reaction rates for the different steps changed with concentration. In the case of k_1 and k_3, curves present a maximum at $C_{H_2O_2} \approx 50\ \mu M$. On the other hand, although k_2 is a monotonously increasing function of the concentration, it presents two regions with different slopes. In this case, the slope change also occurs close to 50 μM. The change in behavior was also evidenced in the calibration curve and in the Electrochemical Impedance Spectra (EIS) measurements[20].

The two constants of the electrochemical steps, k_1 and k_2, are functions of both the overpotential (η) and the concentration ($C_{H_2O_2}$). ST1 (Supporting information) lists k_1, k_2 and k_3 values obtained by the fitting. The kinetic constant functions were interpolated for different concentrations by means of polynomial functions (SE1-SE3). By replacing equations (SE1-SE3), equation (1-3), the current density j is obtained. Figure 5 shows the resulting j surface as a function of time and measured concentration ranges. In all cases, at short times there are large cathodic currents, while after 50 seconds, the stationary current (j_∞) is reached for all concentrations.

3. Atomistic Characterization of the HPRR/surface

3.1 Displacement of H_2O by H_2O_2

In the open circuit potential transients at different concentrations, adsorption of H_2O_2 is observed. As seen initially, the surface has a monolayer of H_2O molecules, which must be displaced to allow adsorption of H_2O_2 according to:

$$H_2O_{2(aq)} + H_2O_{ads}/S \leftrightharpoons (H_2O_2)_{ads}/S + H_2O_{(aq)} \quad (4)$$

until reaching equilibrium at the interface.

3.2 Proposed Mechanisms for HPRR

As seen in the concentration dependence of the kinetic constants and of the open circuit potential measurements, a significant change in the properties of the interface is observed for analyte concentrations close to $50\ \mu M$. Thus, in order to elucidate the HPRR mechanisms on the g-C_3N_4/HOPG surface, two different mechanisms are considered for the two cases of low and high analyte concentration. Both mechanisms are proposed so as to satisfy the assumptions of the kinetic model and, consequently, the transient measurements.

At low concentrations, the reaction takes place in three steps. The first one is the reductive adsorption on a free site (S):

$$H_2O_{2(aq)} + 1e^- + S \overset{k_1}{\rightarrow} (H_2O_2)^{\cdot-}_{ads}/S \quad (5)$$

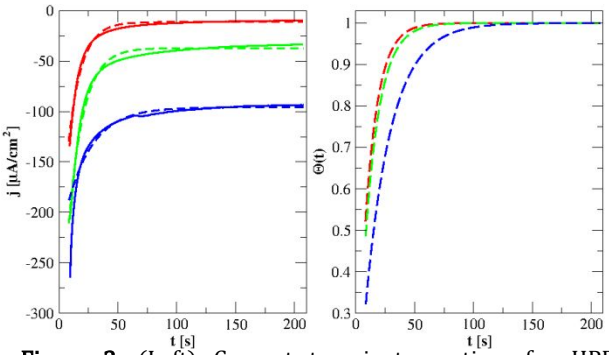

Figure 3. (Left) Current transient vs. time for HPRR. Continuous line refers to experimental data, dashed line refers to data fitted with the proposed kinetic model. (Right) Coverage $\boldsymbol{\theta}$ vs. time for different analyte concentrations: 11.89 μM(red line), 82.64 μM(green line), and 117.65 μM(blue line) of H_2O_2.

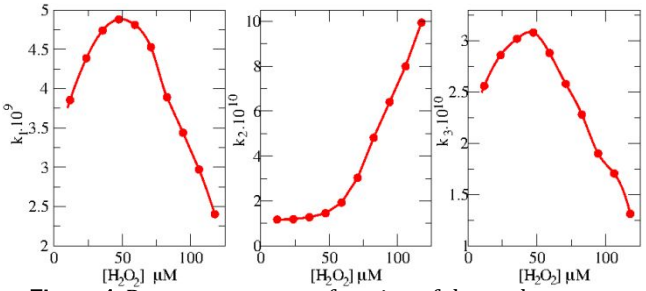

Figure 4. Rate constants as a function of the analyte concentration for the different steps of the HPRR mechanism obtained by fitting of the current / time transients.

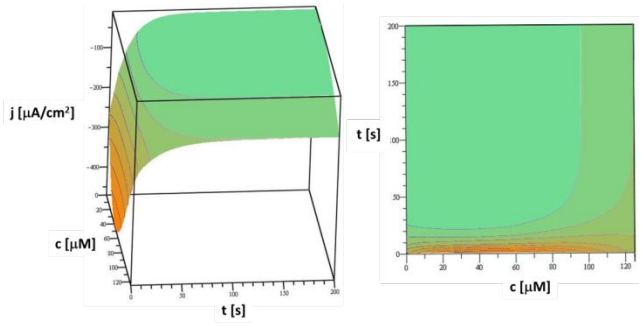

Figure 5.(Left) Current density surface ***j*** for HPRR as a function of concentration and time. (Right) ***j*** iso-surface.

The second step takes place on an occupied site. It is the reductive cleavage of the O-O bond and release of $HO^-_{(aq)}$:

$$(H_2O_2)^{\cdot}_{ads}/S + 1e^- \xrightarrow{k_2} (HO)^-_{ads}/S + HO^-_{(aq)} \quad (6)$$

The third step is the release of the site. An HO^- ion is desorbed:

$$(HO)^-_{ads}/S \xrightarrow{k_3} S + HO^-_{(aq)} \quad (7)$$

At high concentrations there is greater order in the double layer, probably composed of two layers of H_2O_2 next to the surface. This ensures a quick adsorption even before the site is released, thus explaining the decrease of the kinetics of site release ($k_3\downarrow$) and the increase of the kinetics on occupied site ($k_2\uparrow$). As a result, the mechanism occurs in two steps on an occupied site.

The first step is the H_2O_2 simultaneous reductive adsorption on an occupied site ($S' = (HO)^-_{ads}/S$), cleavage of the O-O bond and release of $HO^-_{(aq)}$:

$$H_2O_{2(aq)} + 1e^- + (HO)^-_{ads}/S \xrightarrow{k_2'} (HOHO)^{\cdot}_{ads}/S + HO^-_{(aq)} \quad (8)$$

The second reductive step is the release of a second $HO^-_{(aq)}$ with the breaking of an H-bond interaction.

$$(HOHO)^{\cdot}_{ads}/S + 1e^- \xrightarrow{k_2''} (HO)^-_{ads}/S + HO^-_{(aq)} \quad (9)$$

The two mechanisms have allowed us to explain why the Faradaic process passes from a diffusional to a resistive control[20]. The diffusional control implies that the kinetics is limited by the arrival of the H_2O_2 at the surface while the resistive control indicates that the reaction is limited by the resistance of the electrode to supply electrons.

3.3 Adsorption of the Different Species

To verify the stability of different adlayer structures on the surface, we first studied the properties of different adsorption species present at the interface. Consistently with our kinetic model and with the experimental pH and potential, most of the simulated species and interfaces involve negatively charged systems. This poses some additional challenges to simulations, as plane-wave-based DFT approaches are known to fail to correctly localize the additional electrons[42]. In particular, self-interaction errors of standard flavors of DFT lead to unbound HOMO levels for anions, with the net result that an anion approaching a substrate will likely transfer part of its additional charge to the substrate even for large separations[43]. Self-interaction correction schemes, such as the use of hybrid functions or the recently proposed use of embedding approaches[44], could help in converging the simulations. However, at the present stage we decided to focus on the analysis of the configurational and geometrical effects linked to the alternative reaction pathways, thus neglecting the possible source of inaccuracies due to the unphysical delocalization of the negative charge of the systems.

Even though the adsorption may be affected by the structure of the electrochemical double layer, in our initial analysis we only considered the environment in terms of its electrostatic screening, as effectively captured by describing the solvent as a continuum dielectric medium. This approach allows us to include the main electrostatic screening of the solvent on the electro-catalytic system, without requiring to explicitly perform the statistical sampling of the solvent configurations. We adopted the recently proposed SCCS model by Andreussi *et al.*[32], knowing that its original parameterization could reproduce experimental solvation free energies of neutral organic molecules in water with a mean accuracy of 0.05 eV. In line with similar continuum approaches in the literature, a worse agreement with experiments has been reported for negatively charged systems (anions), for which a re-parameterization of the model was proposed[45].Considering that in the following we will analyze both neutral and anionic systems, only the original parameterization has been taken into account. Yet, thorough evaluations of its effects have been performed.

Table 1 shows the adsorption energies, E_{ads}, inter-atomic distances and atomic charges for: **1)** adsorption of H_2O_2 on a free N_2 site (S); **2)** reductive adsorption of H_2O_2 on S; **3)** reductive adsorption of H_2O_2 on an occupied site (S'); and **4)** H_2O adsorption on S. Figure 6 shows the optimized geometry of species 2-4 on the surface. It is evident from the reported figures that all of these adsorption processes produce corrugation of the outermost substrate sheet as well as a more or less pronounced modification of the inter-planar distances.

In all cases, H-bond interactions play a crucial role. On S, the oxygen atom of H_2O_2 acts as H-bond donor towards the nitrogen atom of the substrate's site. The computed adsorption energies of H_2O_2 on S are smaller than on S', but still larger than that obtained for H_2O, thus providing further validation to the mechanism of site replacement observed as the concentration of the analyte increases (eq. 4).

	System	E_{ads}	$d_{X\text{-}H}$	$d_{Y\text{--}H}$	Q_X	Q_H	Q_Y
1	$(H_2O_2)_{ads}/S$	-0.56	1.00	1.97	-0.31	0.34	-0.25
		-0.35	1.00	1.90	-0.36	0.35	-1.25
2	$(H_2O_2)^{\delta-}_{ads}/S$	-2.47	1.00	1.86	-0.35	0.34	-0.28
		-0.44	1.03	1.70	-0.39	0.34	-1.28
3	$(H_2O_2)^{\delta-}_{ads}/S'$	-2.28	1.01	2.12	-0.32	0.36	-0.52
		-0.77	1.00	1.94	-0.35	0.40	-0.55
4	$(H_2O)_{ads}/S$	-0.58	0.98	2.52	-0.71	0.34	-0.25
		-0.24	0.99	2.49	-0.69	0.34	-0.25

Table 1. Adsorption energy in eV, d_{X-H} (donor) and d_{Y--H} (acceptor) distances in Å. Q_X; Q_Y; Q_H are the Löwdin's charges in atomic unit of donor, acceptor, and hydrogen atoms. White and light blue backgrounds refer to simulations in vacuum and water environment, respectively.

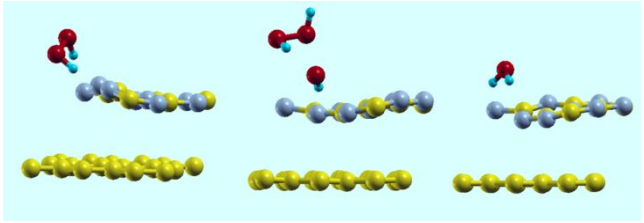

Figure 6. Adsorption of different species on g-C_3N_4/HOPG surface. (Left) reductive adsorption of H_2O_2 on S. (Center) reductive adsorption of H_2O_2 on S'. (Right) adsorption of H_2O on S. C: yellow spheres; N: gray spheres; O: red spheres; H: cyan spheres.

Including the effect of the solvation environment shows a significant change in the absolute values of the adsorption energies, with adsorption on free S site made less favorable, while substantially stabilizing the occupied S' adsorption. Nonetheless, solvation does not affect the overall qualitative picture obtained in vacuum. In particular, also for the solvated systems, H_2O shows the lowest adsorption energy, followed by H_2O_2 adsorption on the S site and eventually by adsorption on the occupied S'site.

Relating the calculated adsorption energies with the experiments, we can say that the adsorption energy of H_2O_2 on S $(-0.35\ eV)$ corresponds to the process observed in the open circuit potential case (section 1), while the reductive adsorption of H_2O_2 on S $(-0.44\ eV)$ corresponds to the process measured when the potential is applied to the electrode (section 2.2). If we assume that the adsorption of the analyte on the surface of the sensor follows a Langmuir-type isothermal behavior[46], we can predict how these changes in adsorption energies will modify the surface coverage, θ, and the ratio of concentrations between the adsorbed species on the surface (C_s) and that in the solution (C_v)(see Supporting Information section). Figure 7 and ST2 comparatively shows how change on E_{ads} modifies what happens on the surface. As in both cases the range of concentration is the same, no changes are expected in the chemical potential of adsorption (μ_{ad}). Indeed, the μ_{ad} plots for both neutral and reductive adsorption (Figure 7 left panels) are equivalent to that of E_{OCP} vs. concentration registered at open circuit potential (Figure 2).

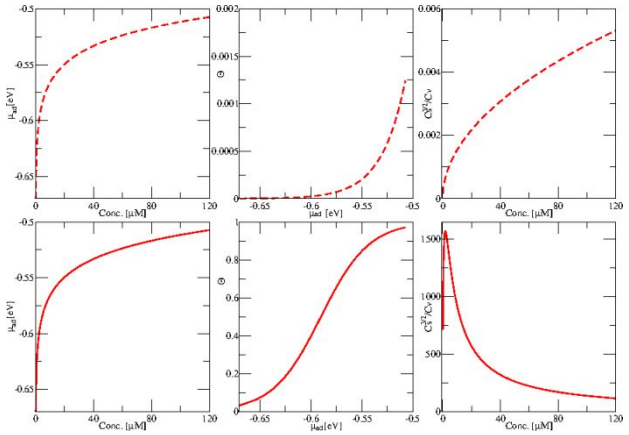

Figure 7. (Top panels) H_2O_2 adsorption (Bottom panels) reductive adsorption of H_2O_2 on S. (Left) μ_{ad} as function of concentration. (Center) θ as function of μ_{ad}. (Right) $C_s^{3/2}/C_v$ ratio as function of concentration.

Instead, surface coverage (θ)(Figure 7, middle panels) stays very low for neutral adsorption process, while going from low to complete covering in the reductive step (see ST2). The last case is in agreement with the coverings observed experimentally in Figure 3 Right.

Moreover, the concentration ratio $(C_s^{3/2}/C_v)$ in the first case presents a monotonically increasing behavior, while in the second case, at low concentration in the 0-50 μM range, there is surface excess, and at higher concentrations a decreasing behavior is observed (Figure 7, right panels).

In section 2.2 (Figure 4 - k_3 constant) a decrease in the kinetics of site release was seen at high concentrations, whereas a considerable increase was found in the kinetics of the HPRR (k_2). This opens the possibility for reductive adsorption on S' (Figure 6 – medium) to take place, which shows an even greater adsorption energy in solution (-0.77 eV), as summarized in Table 1.

3.4 Low Analyte Concentrations

Following the characterization of the alternative adsorption processes on the substrate, analysis of the free energies and reaction barriers connected to the different elementary steps was performed. For this purpose, simulations were performed for individual reactants, products, and transition energy paths of the three catalytic steps proposed (eqs. 5-7) for low analyte concentrations, both in vacuum and in solution. Results are summarized in Table 2. For all simulations, both in vacuum and in solution, the three steps were found to be exothermic. However, the solvation environment is seen to substantially affect the MEP profiles. The kinetic of the reaction changed accordingly, with a significant reduction in the barrier of the Rate Determining Step (RDS) for the direct reaction, passing from 0.80 eV (vacuum) to 0.19 eV (water). Eventually, the free energy change of the whole HPRR ranged from a value of -11.04 eV (vacuum) to a value of -6.69 eV (water).

Environ	Step 1		Step 2		Step3		ΔG_{total}
	E_{b_1}	ΔG_1	E_{b_2}	ΔG_2	E_{b_3}	ΔG_3	
Vacuum	→ 0.00 ← 2.47	-2.47	→0.80 ←4.82	-4.02	→ 0.08 ←4.63	-4.55	-11.04
Water	→ 0.12 ← 0.56	-0.44	→0.19 ←3.62	-3.43	→ 0.03 ←2.84	-2.81	-6.69

Table 2. HPRR on N_2 site of g-C_3N_4/HOPG at low analyte concentrations. Activation energy barrier (E_{bi}); free energy difference (ΔG_i) and total free energy difference (ΔG_{total}), in eV.

The above thermodynamic results should be compared to the experimental value of the electrochemical process, as estimated from standard redox potentials and corrected to account for concentration and applied potential effect. In particular, in standard conditions, i.e. when the concentration of H_2O_2 is 1M and the concentration of H^+ is 1M (pH 0), we expect the free energy change for the HPRR to be equal to zero when the applied electrochemical potential is equal to the redox potential of H_2O_2, i.e. if $U = 1.776V$[47] vs. SHE (i.e. $U = 6.216V$ in an absolute scale, using $U^{SHE} = 4.440V$[48] as reference). As the environment conditions change, we expect

the free energy of the process to vary according to the following relation

$$\Delta G = \Delta G^0 - k_B T ln\frac{[H_2O_2]}{1M} - 2k_B T ln(10) pH + 2eU. \quad (10)$$

More details on the derivation of the above equation are reported in the Supporting Information (SI 3).

For the experimental setup, where pH 7, the concentration of H_2O_2 is of the order of $10 - 100\mu M$, the applied potential is $U^{WE} = -0.6\ V$ vs. $Ag/AgCl$ ($U^{Ag/AgCl} = 0.197\ V$[49] vs. SHE, thus the applied potential is $U^{WE} = -0.403\ V$ vs. SHE or $U^{WE} = 4.037\ V$ in the absolute scale), the free energy of the process is within the range $[-5.483,\ -5.424]\ eV$.

Comparing the computed free energy differences with the experimental results would require to explicitly account also in the simulations for the effects of the electrochemical environment, namely in terms of the applied potential and pH. As the reported results only refer to a specific charge state of the system and to a specific number of hydroxyl ions in the simulation cell, a direct connection between the simulated conditions and the experiments cannot be inferred. From the thermodynamic perspective, an approach analogous to the computational hydrogen electrode (CHE) or, preferably, to the grand potential approach proposed by Hörmann and coworkers[50], would allow to provide a more accurate comparison between theory and experiments. However, the significant improvement obtained with the solvated simulations and the relative agreement with the expected experimental free energies validate the use of the reported analysis for a qualitative understanding of the electrocatalytic mechanism and of the role of the electrode material.

In particular, as seen in the adsorption processes, the corrugation of the outermost sheet of the substrate and the inter-planar interaction in the electrode material appears to have a profound effect in the catalytic mechanisms. This phenomenon occurs on any site of the sheet; yet, it is more evident on the preferential site, which is next to a pore. In this case, the lone pair is a sp^2 orbital located on the xy plane. Thus, the sheet has to corrugate so that H-bond interaction takes place. The corrugation of this sheet modifies aromaticity, decreases van der Waals interactions and increases inter-planar distance.

To further characterize the atomistic details of the electro-catalytic process and the effects of the different steps on the substrate structures, an analysis of the inter-planar distance as a function of the reaction coordinates was performed. As a useful and intuitive parameter to understand the movement of the sheets (curvature, displacement, etc.) in the substrate, we introduced d_{ij} as a radio between average inter-planar distance $\overline{d}_{ij}$ and expected distance d_e as:

$$d_{ij} = \frac{\overline{d}_{ij}}{d_e} \quad with \quad d_e \begin{cases} 3.20\ \text{Å} & if \quad i = 1 \\ 3.35\ \text{Å} & if \quad i \neq 1 \end{cases} \quad (11)$$

Where the reference distances are the ones obtained for the pristine electrode and reported in Figure 1. Figure 8 shows some relevant geometry along the MEPs, as well as the behavior of the inter-planar distances for the first three layers of the substrate.

Step 1 corresponds to reductive adsorption process (eq. 5), with the first configuration of the MEP corresponding to the H_2O_2 approximately 7.5 Å away from the negatively charged substrate. The energy decreases monotonically along the MEP in vacuum while presenting an energy barrier of 0.12 eV in water, with ΔG_1 equal to -2.47 eV and -0.44 eV in the two environments, respectively. Continuum dielectric effects are supposed to provide electrostatic stabilization of solvated systems, especially in the case of charged solutes. Still, the de-stabilization observed upon adsorption results from the competition between solvation of the two individual subsystems (substrate and adsorbate) and their direct interaction. Although a larger solvation free energy may be obtained for this system, when using the model's parameters fitted on anions, the overall effect on the free energy difference of the reaction step is estimated to be small.

To better characterize the mechanism of the reductive adsorption step and the possible limitations due to the unphysical electron delocalization, the charge distribution of the system was analyzed using Löwdin's approach. In the Supporting Information (Figure SF1 and Table ST3) the histograms of Löwdin's charges (a.u.) as a function of the direction orthogonal to the substrate is reported for the first and the last images of the NEB simulation. All the graphene sheets were negatively charged while the g-C_3N_4 sheet, due to the binary composition, had a large in-plane variability and net charge close to zero. As expected, part of the negative charge of the system is already transferred to the peroxide molecule in the first image of the MEP. The final configuration of the path, where the peroxide molecule is fully optimized on the substrate, shows a partial reduction of the molecule, with a negative charge of 0.17 and 0.25 a.u. in vacuum and in solution, respectively. The occurrence of unphysical charge delocalization induced by the DFT self-interaction error alter the energetics of the first step, leading to a significantly reduced energy difference with respect to the thermodynamic limit (Table 2), as obtained from simulations on infinitely separated systems. However, the effect has a similar magnitude in vacuum and in the dielectric environment, suggesting a qualitative picture of a barrier-less reductive adsorption.

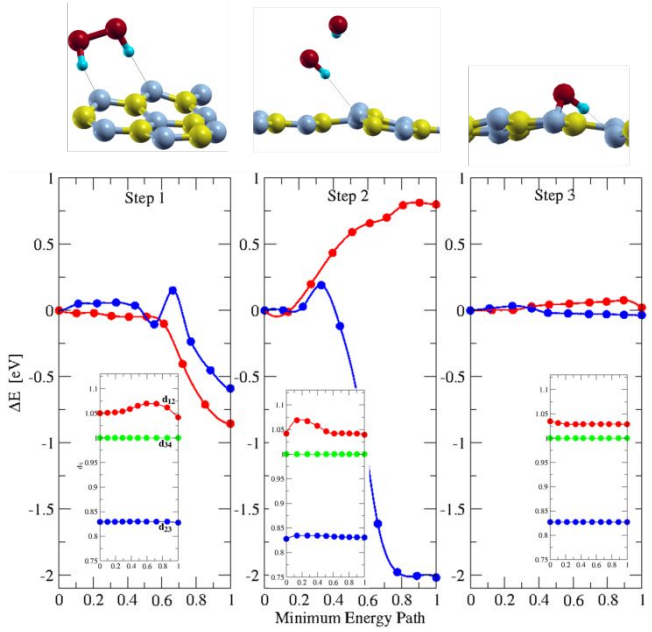

Figure 8. HPRR on g-C_3N_4/HOPG on ***S*** site at low analyte concentrations. (Left) Step 1; (Medium) Step 2; (Right) Step 3. (Up) Relevant geometries of each step at substrate/water interface. C: yellow spheres; N: gray spheres; O: red spheres; H: cyan spheres. (Down) Minimum Energy Paths for each step. Reaction in vacuum (red line), reaction in water (blue line).

(Inset) Interplanar distances between planes i and j, $\boldsymbol{d_{ij}}$: first/second, $\boldsymbol{d_{12}}$ (red); second/third, $\boldsymbol{d_{23}}$ (blue); third/fourth, $\boldsymbol{d_{34}}$ (green).

Analyzing the inter-planar distances, it is evident that the negative charge in the substrate is responsible for a significant geometrical change in the two outermost layers, with the g-C_3N_4 layer moving away from the graphitic substrate. The increase in the d_{12} parameter can be associated with the structural changes required by the formation of the H-bond interaction charge transfer process between the substrate and the redox species. To compensate for the reduced van der Waals interaction with the g-C_3N_4, the topmost graphite layer gets closer to the underlying layers. However, no significant changes with respect to the pristine substrate are observed for the rest of the graphite layers. In addition to the modifications due to the overall charge state of the system, the transition state associated with the adsorption of H_2O_2 shows a significant corrugation of the outermost sheet of the surface.

Table 3. Net charges (in a.u.) on substrate and adsorbate for the reductive adsorption of H_2O_2 on g-C_3N_4/HOPG.

Step 1	Substrate		H_2O_2	
	Vacuum	Water	Vacuum	Water
Reactants	-1.000	-1.000	0.000	0.000
Products	-0. 831	-0.749	-0.169	-0.251

Following peroxide adsorption, step 2 (eq. 6) requires the reductive cleavage of the O-O bond, which represents the RDS for the whole catalytic process. At the end of this process, one hydroxide ion remains on the surface while the second one moves away from the substrate. The direct reaction in vacuum has a barrier of 0.80 eV: breaking of the O-O bond requires energy, but as the negative charge in the system increases, releasing a negative ion from the surface provides a strong driving force for the process, resulting in $\Delta G_2^{vacuum} = -4.02$ eV (Table 2). When this step takes place in water, the MEP profile changes due to the extra stabilization of the hydroxyl anion surrounded by the continuum water, providing a final free energy difference of $\Delta G_2^{water} = -3.43$ eV (Table 2). Even though the thermodynamic force of this step is reduced by the presence of the environment, kinetics appears to be favored by solvation, with a substantial decrease in the energy barrier. Also in this case, delocalization of the negative charges in the system along the MEP calculations may affect the overall quantitative agreement with the experiments, possibly reducing the simulated energy barriers.

Eventually, in step 3 (eq. 7), desorption of the second OH^- takes place. Table 2 shows the activation barrier for desorption: 0.08 eV (in vacuum) and 0.03 eV (in water). Although there were geometric changes (corrugation) in substrate plus electronic transfer process involved in hydroxyl desorption, the superposition of these effects took place with an almost insignificant energy barrier. The thermodynamics of the process shows a strong effect due to the solvent, specular to the effect observed for the first step of reductive adsorption. When compared to the adsorption step, the free energy difference of hydroxyl desorption reflects the different binding strengths between hydroxyl/peroxide and the substrate. Similarly to what was observed for the adsorption step, Löwdin's charge analysis of the MEP simulation of OH desorption shows that the topmost layer of the substrate has the largest changes in charge state, going from a small negative to a positive partial charge. While this change is consistent in the simulations in vacuum and in solution, also in this process a significant delocalization error affects the system. In particular, as shown in the Supporting Information (Table ST4), only a fraction of the additional electron in the system is eventually localized in the hydroxyl group in vacuum, while the simulation in solution shows a qualitatively more realistic result, consistent with the capability of the dielectric embedding environment of overcoming the unbound anion problem[43]. Also in this case, a qualitative barrier-less process can be inferred from the MEP simulations. Substrate reorganization appear to be moderate in this step, with the inter-planar distances normalizing as the adsorbate hydroxyl group is released (inset of right panel of Figure 8).

Step 3	Substrate		HO	
	Vacuum	Water	Vacuum	Water
Reactants	-0.856	-0.824	-0.144	-0.176
Products	0.000	0.000	-1.000	-1.000

Table 4. Net charges(in a.u.) on substrate and adsorbate for desorption of $HO^{\delta-}$ from g-C_3N_4/HOPG surface.

3.5 At High Analyte Concentrations

As discussed above in the analysis of the rate constants obtained from the fitting of current transients with the kinetic model (Figure 4), a change on the kinetic behavior of the reaction at high concentrations is observed. Despite the fact that the number of free sites decreases with concentration, the process kinetics increases. In order to be able to explain this counter intuitive behavior, an alternative mechanism must play a role in the observed processes.

The alternative two-step mechanism proposed in eqs. 8-9 occurs on an occupied site (S'). Table 5 and Figure 9 show simulation results on the thermodynamic and kinetic properties of this mechanism. In this mechanism, both in vacuum and in water, the two steps were exothermic. However, while an energy barrier is observed in vacuum for the first step, both processes appear to be barrier-less in the dielectric solvent model. Therefore, this first step can be identified as the RDS in vacuum, while a spontaneous reaction is predicted in a continuum solvent. Concerning the structural changes that occur in the substrate during these two steps, only minor effects on the inter-planar distances are observed. As these processes take place on an already occupied catalytic site (S'), the corrugation of the outermost sheet of the substrate is not significantly affected by the reductive process. This contributes in reducing the energy barrier for these steps, as opposed to the low-analyte situation, where an activated substrate deformation upon adsorption was shown to be present.

Environment	Step1		Step 2		ΔG_{total}
	E_{b1}	ΔG_1	E_{b2}	ΔG_2	
Vacuum	→ 0.30 ←2.39	-2.29	→0.00 ←7.01	-7.01	-9.30
Water	→ 0.00 ←0.77	-0.77	→0.00 ←5.82	-5.82	-6.59

Table 5. HPRR on N2 site of g-C_3N_4/HOPG at high analyte concentrations. Activation energy barrier (E_{bi}); free energy difference (ΔG_i); and total free energy difference (ΔG_{total}), in eV.

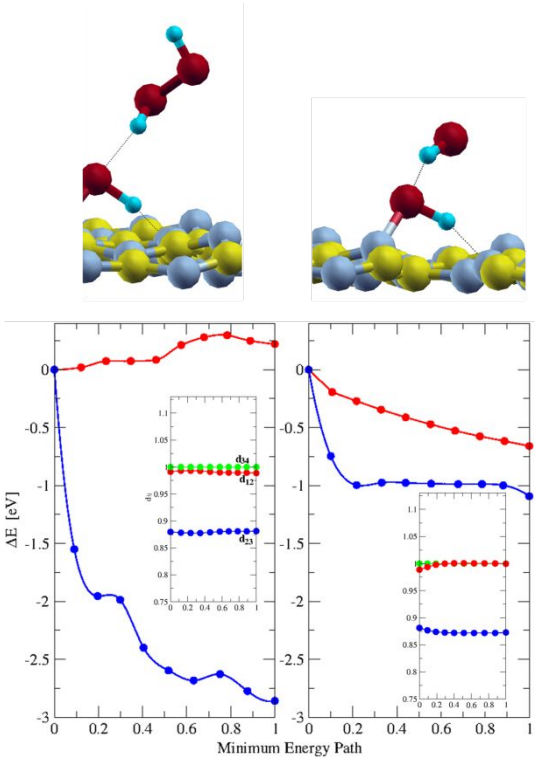

Figure 9. HPRR on g-C_3N_4/HOPG on S' site at low analyte concentrations. (Left) Step 1; (Right) Step 2. (Up) Relevant geometries of the stepsat substrate/water inter-face. C: yellow spheres; N: gray spheres; O: red spheres; H: cyan spheres. (Down) Minimum Energy Paths for each step. Reaction in vacuum(red line), reaction in water(blue line). (Inset) Interplanar distances between planes i and j, d_{ij}: first/second,d_{12} (red); second/third, d_{23} (blue); third/fourth, d_{34} (green).

CONCLUSIONS

The $g-C_3N_4/HOPG$ electrode is an outstanding sensor for the detection and quantification of hydrogen peroxide. Among the possible contributions to this enhanced activity, here we analyze its kinetics and the operation mechanism of this electro-catalyst. In the first part of the work, the rate constants of the processes that take place on the surface of the electrode were studied. By fitting the current transients using a kinetic model, it was observed that the kinetics of the HPRR presents a change with the concentration of the analyte. Paradoxically, although the number of free sites decreased, the current density increased considerably. This indicates that a second reaction mechanism came into play at high concentrations.

The two proposed mechanisms were corroborated by first principles simulations, where precise and detailed atomistic descriptions of the processes that take place at the electrode / water interface during the reaction were carried out. A qualitative agreement with experimental thermodynamics allowed us to rationalize the key electronic and structural properties that affect the elementary steps of the two proposed mechanisms and to explain the change in the kinetics of the reaction. Moreover, by performing the simulation in vacuum and in solution, the effects of the electrochemical environment in promoting and reducing the energy barriers of the process was elucidated. Simulations allowed to qualitatively identify a crucial structural aspect of the electro-catalytic process, namely how the corrugation processes in the substrate influenced the stability and kinetics of the reaction. At low analyte concentrations, a significant deformation of the substrate is observed, involving the reduction of the van der Waals interaction in the substrate layers that facilitate the adsorption and dissociation processes. At high concentrations, adsorption began to occur at an occupied site and, therefore, no corrugation effects were observed in the substrate sheets during the two steps, leading to spontaneous reactions. This second mechanism gained prominence at higher concentrations because the adsorption takes place on an occupied site.

The capability of this system to balance between relatively weak inter-layer interactions and hydrogen bonding interactions with the adsorbate appears to be crucial for allowing the electrochemical process to occur. The ease with which the two interactions can be adjusted and the low activation barriers involved may represent a hidden feature common to other layered systems and van der Waals heterostructures, supporting their promising role as electrocatalysts.

ASSOCIATED CONTENT

Supporting Information

The Supporting Information is available free of charge on ASC Publications website at DOI xxxxx.

List of kinetic constants and polynomial interpolation as function of concentration. Deduction of coverage; $C_s^{3/2}/C_v$ as a function of concentration and Table at two different adsorption energies (-0.35 eV; -0.59 eV). Computational Hydrogen Electrode Approach for Electro-Catalytic Free Energies.

Charge Distribution along NEB Simulations at Low Analyte Concentrations.

AUTHOR INFORMATION

Corresponding Author

*mrojas@fcq.unc.edu.ar

ORCID

Mariana I. Rojas: 0000-0002-1990-761X
Oliviero Andreussi: 0000-0002-1869-5678
Cesar G. Gomez: 0000-0001-6625-399X
Lucía B. Avalle: 0000-0003-2773-4023

Notes

The authors declare no competing financial interest.

ACKNOWLEDGMENT

Authors acknowledge financial support from Consejo Nacional de Investigaciones Científicas y Técnicas (CONICET) though Grant PIO159201501000l3CO and SeCyT-UNC 33620180100222CB. This work used computational resources from CCAD, Universidad Nacional de Córdoba, in particular Mendieta Cluster, which is part of SNCAD-MinCyT, República Argentina. The authors also wish to thank language assistance by C. Mosconi.

REFERENCES

(1) Terry, L.A.; White, S.F.; Tigwell, L.J. The Application of Biosensors to Fresh Produce and the Wider Food Industry.*J. Agric. Food Chem.***2005**, 53, 1309-1316.

(2) Bai, J.; X. Jiang, X.A Facile One-pot Synthesis of Copper Sulfide-Decorated Reduced Graphene Oxide Composites for Enhanced Detecting of H2O2 in Biological Environments. Analytical Chemistry **2013**, 85, 8095-8101.

(3) Du, P.; Wu, P.; Cai, C. A glucose biosensor based on electrocatalytic oxidation of NADPH at single-walled carbon nanotubes functionalized with poly(nile blue A).*J. Electroanal. Chem.***2008**, 624, 21-26.

(4) Wang,*J.*Electrochemical Glucose Biosensors.*Chem. Rev.***2008**, 108, 814-825.

(5)Jin, H.; Heller, D.A.;Kalbacova, M.; Kim, J.; Zhang, J.; Boghossian, A.A.; Maheshri, N.;Strano, M.S. Detection of single-molecule H2O2 signaling from epidermal growth factor receptor using fluorescent single-walled carbon nanotubes.*Nature nanotechnology***2010**, 5, 302-309.

(6)Xie, F.; Cao, X.; Qu, F.;Asiri, A.M.; Sun,X.Detection of single-molecule H_2O_2signaling from epidermal growth factor receptor using fluorescent single-walled carbon nanotubes Cobalt nitride nanowire array as an efficient electrochemical sensor for glucose and H_2O_2 detection. *Sensor and Actuators B***2018**, 255, 1254-1261.

(7) Jamal, M.; Hasan, M.; Mathewson,A.;Raseeb,K.Non-Enzymatic and Highly Sensitive H2O2 Sensor Based on Pd Nanoparticle Modified Gold Nanowire Array Electrode.*Journal of The Electrochemical Society***2012**, 159, B825-B829.

(8)Kachoosangi, R.T.; Compton, R.A simple electroanalytical methodology for the simultaneous determination of dopamine, serotonin and ascorbic acid using an unmodified edge plane pyrolytic graphite electrode.*Anal. Bioanal. Chem.***2007**, 387, 2793-2800.

(9)Woon, H.S.; Durkan, C.; Chandrasekhar, N.Tailoring the local interaction between graphene layers in graphite at the atomic scale and above using scanning tunneling microscopy. *ACSNANO***2009**, 3, 3455-3462.

(10) Wong, H.S.; Durkan,C.Unraveling the rotational disorder of graphene layer in graphite. *Physical Review B***2010**, 81, 45403 (2010).

(11) Novoselov,K.S.;Geim, A.K.; Morozov, S.V.; Jiang, D.; Zhang, Y.; Dubonos, S.V.Electric Field Effect in Atomically Thin Carbon Films.*Science* **2004**, 306, 666.

(12) Dai,H.Carbon nanotubes: opportunities and challenges.*Surface Science***2002**, 500, 218-241.

(13) Kosynkin, D.V.; Higginbotham,A.L.;Sinitskii, A.;Lomeda, J.R.;Dimiev, A.; Price, B.K.; Tour, J.M.Longitudinal unzipping of carbon nanotubes to form graphene nanoribbons.*Nature***2009**, 458, 872–876.

(14) Higginbotham,A.L.;Kosynkin, D.V.;Sinitskii, A.; Sun, Z.; Tour, J.M.Lower-Defect Graphene Oxide Nanoribbons from Multiwalled Carbon Nanotubes.*ACS NANO***2010**, 4, 2059–2069.

(15) Thomas, A.; Fisher,A.;Goettmann, F.;Antonietti, M.; Oliver Müller, J.; Schlögl, R.; Carlsson, J.M.Graphitic carbon nitride materials: variation of structure and morphology and their use as metal-free catalysts.*J. Mater. Chem.***2008**, **18,** 4893-4908.

(16) Azofra, L.M.; MacFarlane, D.R.; Sun, C. A DFT study of planar vs. corrugated graphene-like carbon nitride (g-C3N4) and their role in the catalytic performance of CO2 conversion.*Phys. Chem. Chem. Phys.***2016**, 18, 18507-18514.

(17) Li, X.; Dai, Y.; Ma, Y.; Han, S.; Huang, B. Graphene/g-C3N4 bilayer: considerable band gap opening and effective band structure engineering.*Phys. Chem. Chem. Phys.***2014**, 16, 4230-4235.

(18) Thomas, A.; Fischer,A.;Goettmann, F.;Antonietti, M.; Oliver Müller, J.;Schlögl, R.; Carlsson, J.M.Graphitic carbon nitride materials: variation of structure and morphology and their use as metal-free catalysts.*J. Mater. Chem.***2008**, 18, 4893-4908.

(19) Silva, A.M.; Rojas, M.I.Electric and Structural properties of Polymeric Graphite Carbon Nitride (g-C3N4): A Density Functional Theory Study.*Computational and Theoretical Chemistry***2016**, 1098, 41-49.

(20) Gomez, C.G.; Silva, A.M.; Strumia, M.C.;Avalle, L.B.; Rojas, M.I. The origin of high electrocatalytic activity of hydrogen peroxide reduction reaction by g-C3N4/HOPG sensor.*Nanoscale***2017**, 9, 11170-11179.

(21) Tian, J.; Liu, Q.; Ge, C.; Xing, Z.;Asiri, A.M.; Al-Youbi A.O.; Sun,X.Ultrathin graphitic carbon nitride nanosheets: a low-cost, green, and highly efficient electrocatalyst toward the reduction of hydrogen peroxide and its glucose biosensing application.*Nanoscale***2013**, 5, 8921-8924.

(22)Bieri, M.; Terrier, M.; Cai, J.;Aït-Manssur, K.;Ruffieux, P.; Gröning, O.;Gröning, P.; Kastler, M.; Rieger, R.; Feng, X.;Müllen, K.;Fasel, R. Porous graphenes: two-dimensional polymer synthesis with atomic precision.*Chem. Commun.***2009**, 45, 6919-6921.

(23) Luque, G.L.; Rojas, M.I.; Leiva, E.P.M. The Origin of the catalysis of hydrogen peroxide reduction by functionalized graphene surfaces: A density functional theory study.*ElectrochimicaActa***2010**, 56, 523-530.

(24) Andreussi, O.; Fisicaro, G. Continuum embedding in condensed-matter simulations.*International Journal of Quantum Chemistry***2019**, 119, e25725.

(25)GiannozziP. et al. Quantum ESPRESSO: a modular and open-source software project for quantum simulations of materials.*J. Phys.: Condens. Matter***2009**, 21, 395502.

(26)Giannozzi P. et al. Advanced capabilities for materials modelling with Quantum ESPRESSO.*J. Phys.: Condens. Matter***2017**, 29,465901.

(27)Perdew, J.P.; Burke, K.; Ernzerhof, M.Generalized Gradient Approximation Made Simple.*Phys. Rev. Lett.***1996**, 77, 3865.

(28) Kleinman, L.; Bylander, D.M. Efficacious Form for Model Pseudopotentials.*Phys. Rev. Lett.***1982**, 48, 1425.

(29)We used the pseudopotentials C.pbe-rrkjus.UPF, N.pbe-rrkjus.UPF, O.pbe-rrkjus.UPF and H.pbe-rrkjus.UPF from http://www.quantum-espresso.org.

(30)Monkhorst, H.J.; Pack, J.D.TheMonkhorst and Pack grids.*Phys. Rev. B.***1976**, 13, 5188.

(31)Henkelman, G.; Uberuaga, B.P.; Jónsson, H. A climbing image nudged elastic band method for finding saddle points and minimum energy paths. *J. Chem. Phys.* **2000**, 113, 9901.

(32) Henkelman,G.; Jónsson, H. Improved tangent estimate in the nudged elastic band method for finding minimum energy paths and saddle points. *J. Chem.Phys.* **2000**, 113, 9978.

(33) Sheppard, D.; Xiao, P.; Chemelewski, W.; Johnson, D.D.; Henkelman, G. A generalized solid-state nudged elastic band method. *J. Chem. Phys.***2012**, 136, 74103.

(34) Andreussi, O.; Marzari, N. Electrostatics of solvated systems in periodic boundary conditions. *Phys. Rev. B* **2014**, 90, 245101.

(35) Andreussi, O.; Dabo, I.; Marzari, N. Revised self-consistent continuum solvation in electronic-structure calculations.*J. Chem. Phys.* **2012**, 136, 136.

(36) Fiscaro, G.; Genovese, L.; Andreussi, O.; Marzari, N.;Goedecker, S. A generalized Poisson and Poisson-Boltzmann solver for electrostatic environments. *J. Chem. Phys.***2016**, 144, 014103.

(37) Yang, B.; Mao, X.; Pi, L.; Wu, Y.; Ding, H.; Zhang,W.Effect of pH on the adsorption and photocatalytic degradation of sulfadimidine in Vis/g-C3N4 progress.*Environ. Sci. Pollut. Res.***2017**, 24, 8658-8670.

(38) Hernández-Uresti, D.B.; Vázquez, A.; Sanchez-Martinez, D.; Obregón, S. Performance of the polymeric g-C3N4photocatalyst through the degradation of pharmaceutical pollutants under UV-vis irradiation.*Journal of Photochemistry and Photobiology A: Chemistry***2016**, 324, 47-52.

(39) Zhu, B.; Xia, P.; Ho, W.; Yu,J.Isoelectric point and adsorption activity of porous g-C3N4.*Applied Surface Science***2015**, 344, 188-195.

(40)Lv, Y.; Wang, X.; Yu, X.; Zheng, S.; Wang, S.; Zhang, Y.; Du,H.Adsorption behaviors and vibrational spectra of hydrogen peroxide molecules at quartz/water interfaces.*Phys. Chem. Chem. Phys.***2017**, 19, 7054-7061.

(41) Press, W.H.; Teukolsky, S.A.; Vetterling, W.T.; Flannery, B.P. Numerical recipes: the art of scientific computing; 3rd edition, Cambridge University Press, Cambridge, England **2007**, p. 502-507.

(42) Shore, H.B.; Rose, J.H.; Zaremba, E. Failure of the local exchange approximation in the evaluation of the H^- ground state. *Phys. Rev. B* **1977**, 15, 2858-2861.

(43) Kim, M.-C.; Sim, E.; Burke, K. Communication: Avoiding unbound anions in density functional calculations. *J. Chem. Phys.* **2011**, 134, 171103.

(44) Nattino, F.; Dupont, C.; Marzari, N.; Andreussi, O. Extrapolations to Tame Unbound Anions in Density-Functional Theory Calculations. *J. Chem. Theory Comput.* **2019**; https://doi.org/10.1021/acs.jctc.9b00552.

(45) Dupont, C.; Andreussi, O.; Marzari, N. Self-consistent continuum solvation (SCCS): The case of charged systems. *J. Chem. Phys.* **2013**, 139, 214110.

(46) Hill, T.L. Statistical Mechanics. Principles and Selected Applications; Dover Publication, Inc., New York, United States **1986** pp. 124-130.

(47)Lide, D.R., Editor-in-Chief, Handbook of Chemistry and Physics CRC; 80th Edition, 1999-2000.

(48)Trasatti, S. The Absolute Electrode Potential: an Explanatory Note. *International Union of Pure and Applied Chemistry, Pure* & Appl. Chem.**1986**, 58,955-66.

(49) Allen, B.J., Faulkner, L.R. Electrochemical Methods. Fundamentals and Applications, John Wiley & Sons, Canada, 1980, pp. 60-61.

(50) Hörmann, N.; Andreussi, O.; Marzari, N. Grand canonical simulations of electrochemical interfaces in implicit solvation models. *J. Chem. Phys.* **2019**, 150, 041730; https://doi.org/10.1063/1.5054580.

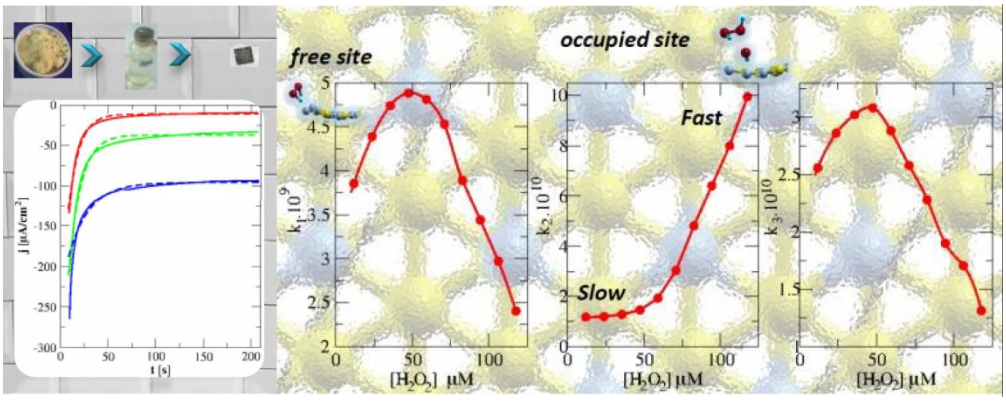

TOC

1021x402mm (96 x 96 DPI)

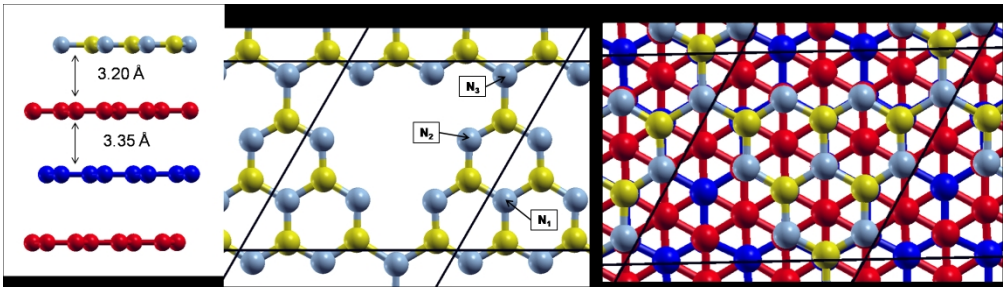

Figure 1

387x109mm (150 x 150 DPI)

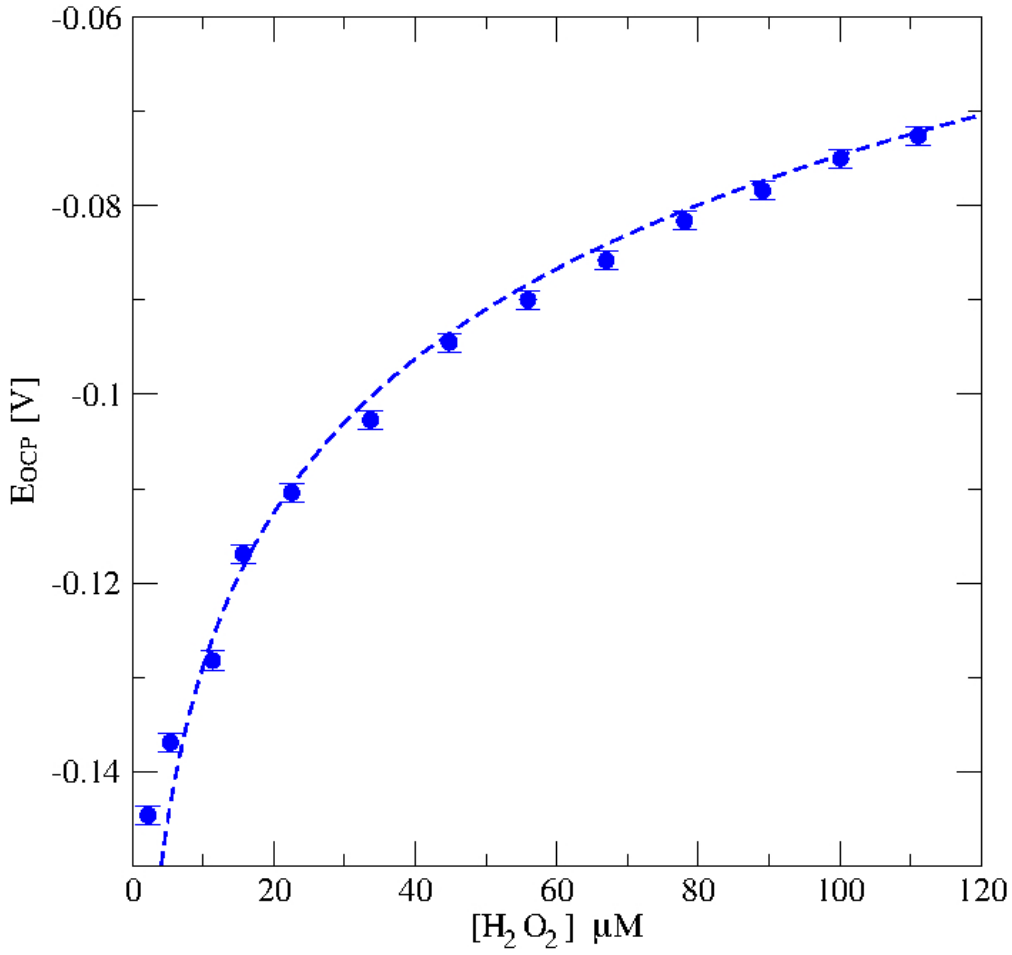

178x168mm (100 x 100 DPI)

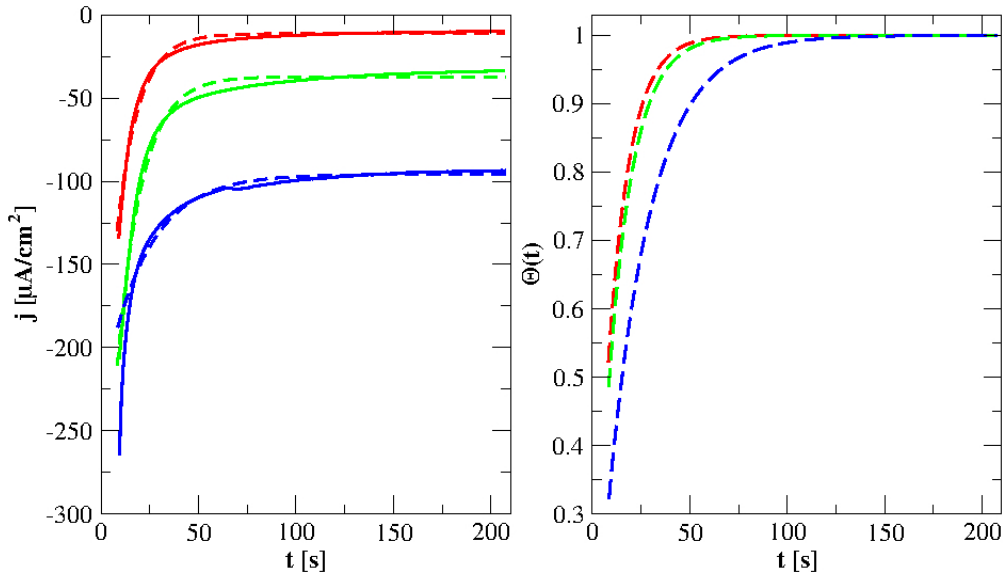
0
-50
-100
-150
-200
-250
-300
j [μA/cm²]
0
50
100
150
200
t [s]
1
0.9
0.8
0.7
0.6
0.5
0.4
0.3
Θ(t)
0
50
100
150
200
t [s]

Figure 3

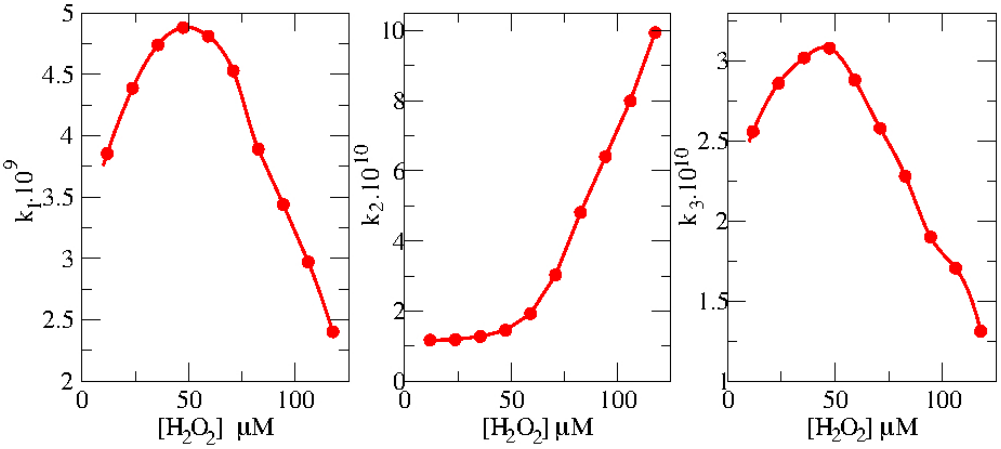

Figure 4

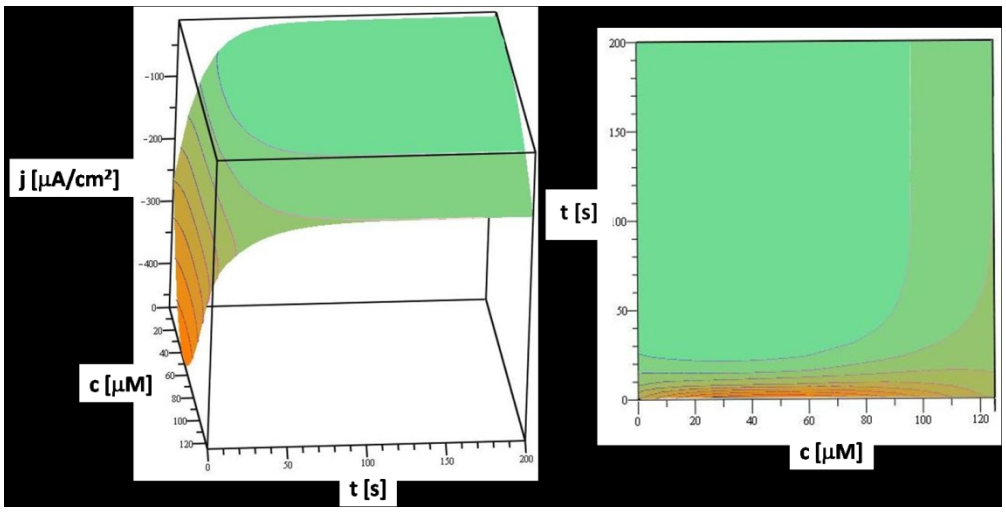

Figure 5

271x135mm (150 x 150 DPI)

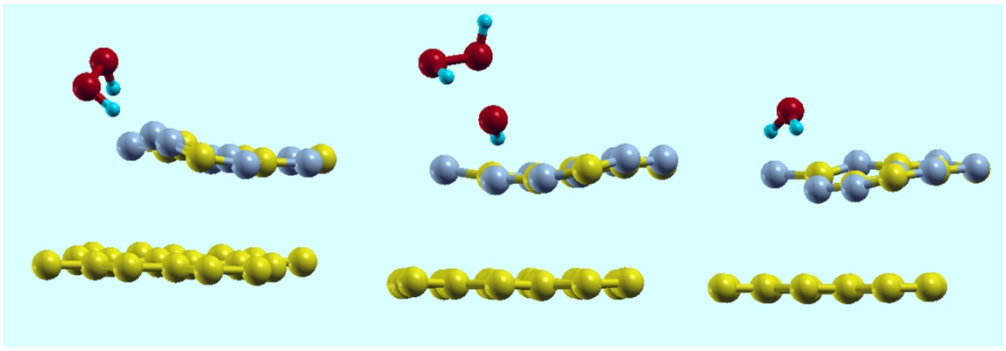

Figure 6

254x87mm (150 x 150 DPI)

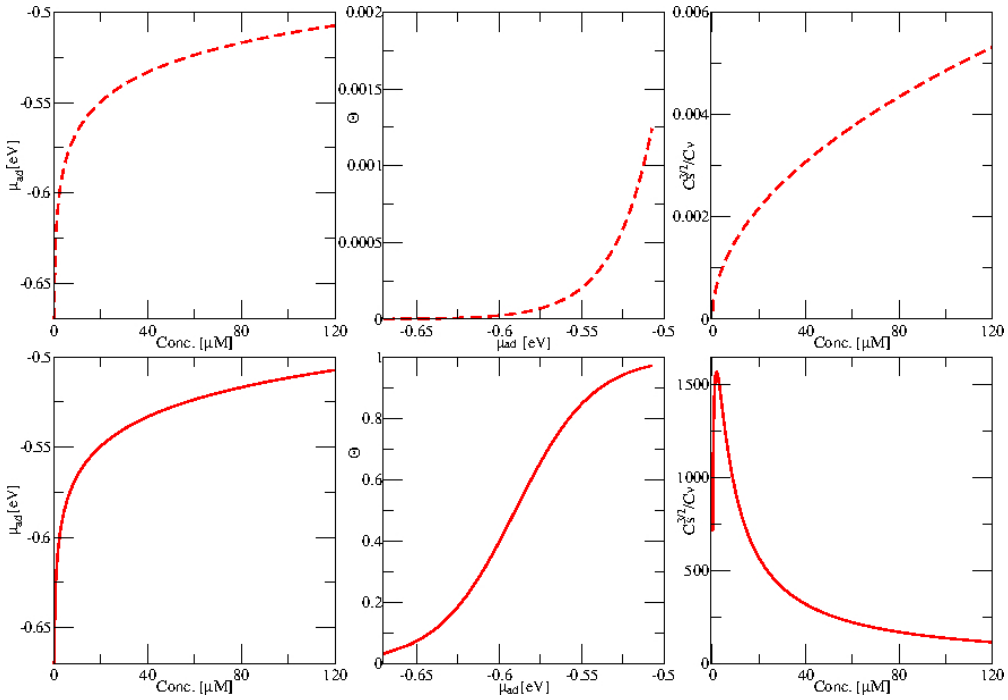

Figure 7

224x154mm (100 x 100 DPI)

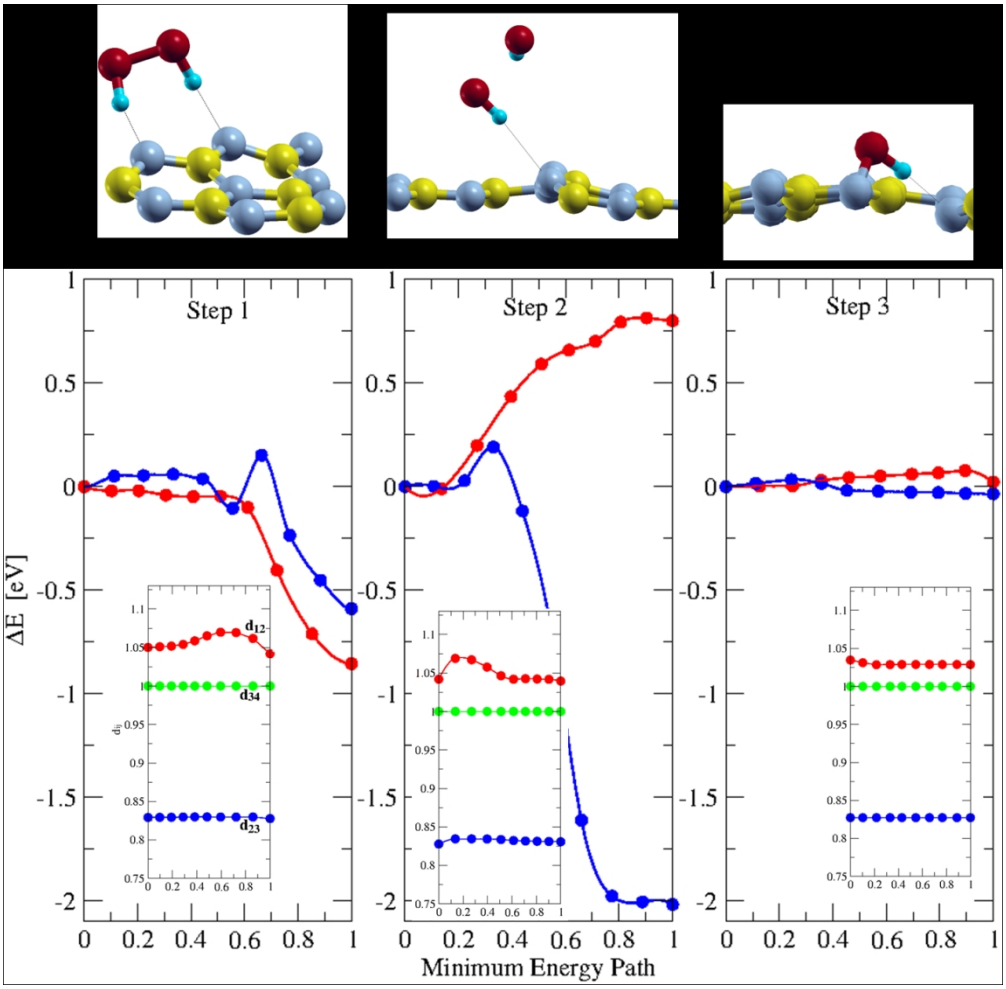

Figure 8

240x235mm (150 x 150 DPI)

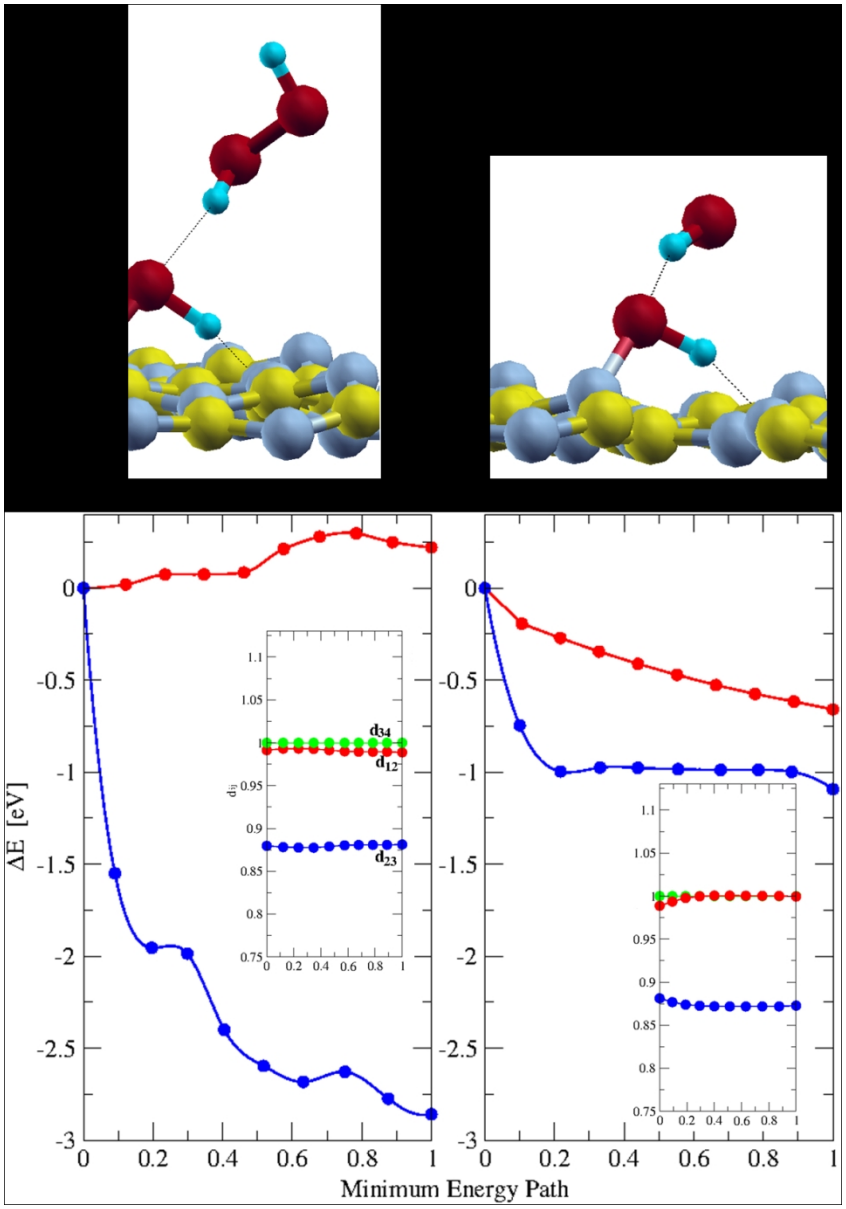

Figure 9

198x284mm (150 x 150 DPI)